Dendritic Growth with Fluid Flow in Pure Materials

JUN-HO JEONG, JONATHAN A. DANTZIG, AND NIGEL GOLDENFELD

We study the growth of a single dendrite from a small initial seed in an undercooled melt in the presence of a forced flow. Three-dimensional models are constructed in which the solidification is computed using an adaptive finite-element mesh and a phase-field method. We compare our calculations with available theories and experiments and conclude that there are significant open questions remaining about the evolution of microstructure when flow is present.

I. INTRODUCTION

DENDRITIC growth is important because it is the basic microstructural pattern in solidified metals. The pattern selected during solidification of a pure material depends on the existing thermal field during freezing. Once this pattern is set, it is difficult to change in the solid state without substantial effort, *e.g.*, through mechanical deformation and heat treatment.

The evolution of dendritic microstructures is reasonably well understood for pure materials growing into undercooled melts under purely diffusive conditions, *i.e.*, when fluid flow is absent. The tip of the dendrite approximates a paraboloid of revolution. Ivantsov[1] determined the solution for the thermal field surrounding an isothermal dendrite, neglecting surface tension, and determined a relation between undercooling and the (constant) tip velocity, V_{tip}, and tip radius, ρ_{tip}, given by $\Delta = I(\text{Pe}_v)$ where Δ is the dimensionless undercooling $(T_m - T_\infty)/(L_f/c_p)$, with T_m as the equilibrium melting point and T_∞ as the far-field temperature, scaled by the characteristic temperature, L_f/c_p, with L_f as the latent heat of fusion and c_p as the specific heat. The term Pe_v is the Péclet number based on the tip radius, defined as $\text{Pe}_v = \rho_{tip}V_{tip}/\alpha$, and α is the thermal diffusivity. The function I is a combination of exponentials and error integrals, whose form is well known and not important for the current discussion. Because the tip radius and velocity appear only as a product, the diffusion solution does not uniquely determine the shape.

The pattern-selection problem is resolved by including surface tension and its anisotropy in the boundary condition for the temperature of the dendrite and by relaxing the assumption that the shape is known.[2,3] This body of theory is known as "microscopic solvability." In two-dimensions, it gives a correction to the shape of the interface near the tip, converging to the Ivantsov solution far away from the tip where curvature becomes negligible. The theory provides a second relation for the dendrite-tip velocity and radius, given by $\sigma^* = 2d_0\alpha/\rho_{tip}^2 V_{tip}$, where σ^* is known as the selection constant, and d_0 is the capillary length, a material constant. The problem is somewhat more complicated in three-dimensions, where corrections to the Ivantsov shape are large. Brener[4] provides a treatment of this problem.

Recent numerical calculations using the phase-field method, in two-dimensions and at high undercooling, agree very well with the predictions of microscopic solvability theory.[5,6] At low undercooling, the computed selection constant, σ^*, still agrees with the theory, but the tip radius and tip velocity differ. Provatas *et al.*[6] showed that this discrepancy arises because the transport solution at low undercooling does not satisfy the premise, assumed in solvability theory, that the dendrite is a single, isolated branch, independent of its neighbors. This may explain the difference between the predictions of microscopic solvability theory and experimental observations, which are invariably made at low undercooling.

The microstructure is significantly altered by the presence of flow during solidification.[7,8] This problem is important because flow induced by buoyancy, residual pouring currents, or forced flow is nearly always present in castings unless great pains are taken to avoid it, for example, by performing experiments in the reduced gravity of outer space. Saville and Beaghton[9] extended the theory of Ivantsov to consider the case of an isolated paraboloid of revolution, with zero surface tension, growing in a shape preserving way at constant velocity, with a uniform forced flow from infinity aligned parallel to the growth axis. The characteristic parameters for this problem are such that the flow is dominated by viscous forces, but the transport is dominated by advection. The flow is, therefore, well approximated by Oseen's equation, and Saville and Beaghton presented a solution where $\Delta = S(\text{Pe}_v, \text{Pr}, \text{Pe}_u)$, where Pr is the Prandtl number for the fluid, and Pe_u is the Péclet number based on the flow, $\text{Pe}_u = U_\infty\rho_{tip}/\alpha$ and U_∞ is the value of the imposed velocity at infinity. Notice that the tip velocity and radius are still not uniquely determined by the transport solution, and a selection criterion is still required.

Bouissou and Pelce[10] examined the stability of a two-dimensional (2-D) dendrite under the assumptions of Saville and Beaghton's analysis and determined the scaling of the selection constant with flow. They presented their results in terms of the function $a(\text{Re})$ given by

$$a(\text{Re}) = \left[\frac{2\text{Re}}{\pi}\right]^{1/2} \frac{\exp(-\text{Re}/2)}{\text{erfo}(\sqrt{\text{Re}/2})} \qquad [1]$$

where Re is the Reynolds number, defined as $\text{Re} = U_\infty\rho_{tip}/\nu$, and ν is the kinematic viscosity. For $a(\text{Re})\text{Pe}_u \ll \text{Pe}_v\rho_{tip}/\Lambda$,

where Λ is the wavelength of a disturbance, assumed to be much smaller than ρ_{tip}, the selection constant σ^* is expected to be independent of the imposed velocity field. In the large velocity limit, i.e., for $a(\text{Re})\text{Pe}_u \gg \text{Pe}_v\rho_{tip}/\Lambda$, Bouissou and Pelcé derived the expression

$$\frac{\sigma_0^*}{\sigma^*} = 1 + b\left[\frac{a(\text{Re})d_0 U_\infty}{15\epsilon_4\rho_{tip} V_{tip}}\right]^{11/14} \qquad [2]$$

where σ_0^* refers to the value of the selection constant in the absence of flow, ϵ_4 is the surface tension anisotropy, and b is a numerical constant.

The applicability of this theory is not yet confirmed by either computations or experiments. A recent study by Beckermann et al.[11] found a weak dependence of the selection constant on flow but neither confirmed nor negated the theory. The existing experimental evidence is also inconclusive and perhaps contradictory. Bouissou et al.[12] examined the flow of a dilute pivalic acid-ethanol (PVA-EtOH) solution past a solidifying PVA dendrite and found a trend similar to that predicted by Eq. [2], i.e., σ^* decreases with imposed velocity, U_∞. On the other hand, in a series of experiments using pure succinonitrile (SCN), Lee et al.[13] found that σ^* increased with U_∞. These discrepancies are currently unexplained, and in this article, we perform simulations intended to shed some light on this issue. We use the phase-field method, which we now describe briefly before proceeding to a more detailed description of our simulations.

The phase-field method has become the method of choice for simulating dendritic growth because of its ability to handle the complex evolving shape of the dendrite.[14–18] Because this method has been described in detail in numerous articles, we present here just a brief sketch. The dendrite-growth problem follows the evolution of the solid from the liquid. In the so-called sharp-interface problem, the liquid/solid interface must satisfy two boundary conditions. Thermodynamic equilibrium requires that the interface temperature, T, satisfy the Gibbs–Thomson condition

$$T = T_m - \Gamma A(\mathbf{n}) - \beta(\mathbf{n})\,\mathbf{V}\cdot\mathbf{n} \qquad [3]$$

where T_m is the equilibrium melting point of the pure material (with a flat interface), Γ is the ratio of the surface energy to the entropy of fusion, $A(\mathbf{n})$ expresses the anisotropy of the surface energy through the weighted mean curvature of the interface (defined further subsequently), $\mathbf{n}$ is the unit vector normal to the interface, β is a kinetic coefficient, and $\mathbf{V}$ is the interface velocity. Crystalline anisotropy is included in the Gibbs–Thomson relation through the function $A(\mathbf{n})$. In the case of cubic symmetry, this function is given by[5]

$$A(\mathbf{n}) = \left(a_s(\mathbf{n}) + \frac{\partial^2 a_s(\mathbf{n})}{\partial\theta^2}\right)\kappa_\theta + \left(a_s(\mathbf{n}) + \frac{\partial^2 a_s(\mathbf{n})}{\partial\phi^2}\right)\kappa_\phi \qquad [4]$$

where θ and ϕ are the usual spherical angles, κ_θ and κ_ϕ are the corresponding curvatures, and

$$a_s(\mathbf{n}) = 1 - 3\epsilon_4 + 4\epsilon_4\,(n_x^4 + n_y^4 + n_z^4) \qquad [5]$$

Finally, ϵ_4 is the measure of the anisotropy in surface tension, γ, often written as $\gamma = \gamma_0(1 + \epsilon_4 \cos 4\theta)$. An energy balance at the interface equates the net heat flux to the latent heat evolved by the moving interface,

$$k_s\,\nabla T_s\cdot\mathbf{n} - k_l\,\nabla T_l\cdot\mathbf{n} = \rho_s L_f\,\mathbf{V}\cdot\mathbf{n} \qquad [6]$$

where the subscripts s and l refer to the solid and liquid

phases, respectively; k is the thermal conductivity; and ρ_s is the solid density.

Solution of the sharp-interface problem for dendritic growth is difficult because it requires that the moving boundary be tracked explicitly. In the phase-field method, a continuous-order parameter $\phi \in [-1, 1]$ is introduced, such that $\phi = -1$ corresponds to the liquid, $\phi = +1$ corresponds to the solid, and the set of locations where $\phi = 0$ corresponds to the interface between the two phases. The liquid/solid interface is diffuse, with nominal thickness W_0. For a more detailed discussion of the method, the specific models used, and a description of convergence of the phase-field model to the sharp interface, see Karma and Rappel,[5] Beckermann et al.[11] and Jeong et al.[19]

The phase-field method introduces an artificial finite width W_0, for the interface. Karma and Rappel[5] demonstrated convergence of the phase-field model to the sharp-interface model in the limit, $W_0 V_{tip}/\alpha \ll 1$, and gave specific formulas for relating the parameters in the two problems. Grid convergence of the numerical solution requires that $\Delta x \sim W_0$ and also that the domain size $L_B \gg \alpha/V_{tip}$. Karma and Rappel[5] provide further details. The important result is that these two requirements force us to choose $L_b/\Delta x \sim 10^3$ or greater. Thus, a uniform mesh would require of the order of 10^6 grid points in two dimensions and 10^9 in three dimensions.

We finesse the length-scale problem by solving the equations on an adaptive grid, providing high resolution near the interface and a coarser mesh further away to resolve the diffusion field. The methods have been described elsewhere,[6,19] and so we provide only a limited discussion in this article in Section II. Plapp and Karma[20] developed a different approach, where they solve the phase-field models on a regular inner grid, and resolve the outer diffusion field using a Monte–Carlo method, with the two solutions matched at an artificial boundary. Both methods are effective for the diffusion problem, but the extension of the latter method to cases where fluid flow is present is not obvious. Accordingly, we focus the rest of our discussion on the solution of the solidification problem with melt convection using our adaptive grid techniques.

It is important to understand that to compare our numerical calculations with experiments, we must perform simulations in 3-D, at low undercooling, and for materials of low anisotropy. Each one of these choices makes the problem computationally more difficult, and the combination represents a formidable challenge. We have developed a code that solves the 3-D Navier–Stokes, energy, and phase-field equations on an adaptive grid in parallel.[19] This is essential for us to take up the problems we have described.

In Section II, we give an abbreviated description of the phase-field model and its numerical implementation. We then describe the results of simulations relevant to the experiments of Lee et al.[13] and Bouissou et al.[12]

II. METHODS

The phase-field method has been extended to include fluid flow in the melt along with solidification.[11,19,21,22] The essential new features, in addition to solving the Navier–Stokes equations in the fluid phase, are the formulation of the model such that the velocity is extinguished in the solid phase and the ensurance that the interfacial shear stress is

correctly represented. Tönhardt and Amberg[21] and Juric[22] use an enhanced-viscosity approach to extinguish the velocity in the solid phase. In this approach, the viscosity, μ, changes rapidly from its value in the melt to a very large value representing the solid, as ϕ goes from -1 to 1. This method is effective, but convergence can be very sensitive to the relative magnitude of the viscosity change and the interface thickness.

We adopt the method of Beckermann et al.[11] who introduced a mixture formulation for the continuity, Navier–Stokes, and energy equations. An interfacial-stress term is added to the Navier–Stokes to ensure that the shear stress is correct at the interface. Beckermann et al.[11] provide further details.

The mixture continuity equation is given by

$$\nabla \cdot \left[\frac{1 - \phi}{2} \mathbf{u} \right] = 0 \qquad [7]$$

where $\mathbf{u}$ is the velocity vector. The phase-averaged momentum equation is

$$\frac{\partial}{\partial t} \left[\left(\frac{1 - \phi}{2} \right) \mathbf{u} \right] + \left(\frac{1 - \phi}{2} \right) \mathbf{u} \cdot \nabla \mathbf{u} + \left(\frac{1 - \phi}{2} \right) \frac{\nabla p}{\rho_0}$$
$$= \nu \nabla^2 \left[\left(\frac{1 - \phi}{2} \right) \mathbf{u} \right] - \nu \frac{h(1 - \phi^2)(1 + \phi)}{8\delta^2} \mathbf{u} \qquad [8]$$

where t is time, p is pressure, ρ_0 is the (constant) density, ν is the kinematic viscosity, $\delta = W_0/\sqrt{2}$ is the characteristic interface width (discussed further subsequently), and h is a constant ($=2.757$), which ensures that the interface shear stress is correct for a simple shear flow (Beckermann et al.[11]).

The phase-averaged energy equation is written in terms of a scaled temperature $\theta = c_p(T - T_m)/L_f$

$$\frac{\partial \theta}{\partial t} + \left(\frac{1 - \phi}{2} \right) \mathbf{u} \cdot \nabla \theta = D\nabla^2\theta + \frac{1}{2} \frac{\partial \phi}{\partial t} \qquad [9]$$

where $D = \alpha\tau_0/W_0^2$ in which α is the thermal diffusivity, W_0 is the interface width, defined further subsequently, and τ_0 is a time-characterizing atomic motion in the interface, also discussed subsequently.

The three-dimensional (3-D) phase-field evolution equation is given by

$$\tau(\mathbf{n}) \frac{\partial \phi}{\partial t} = \nabla \cdot [W(\mathbf{n})^2 \nabla \phi] + [\phi - \lambda\theta(1 - \phi^2)](1 - \phi^2)$$
$$+ \partial_x \left(|\nabla\phi|^2 W(\mathbf{n}) \frac{\partial W(\mathbf{n})}{\partial(\partial_x\phi)} \right) + \partial_y \left(|\nabla\phi|^2 W(\mathbf{n}) \frac{\partial W(\mathbf{n})}{\partial(\partial_y\phi)} \right)$$
$$+ \partial_z \left(|\nabla\phi|^2 W(\mathbf{n}) \frac{\partial W(\mathbf{n})}{\partial(\partial_z\phi)} \right) \quad [10]$$

where λ is a dimensionless constant that controls the tilt of the double-well potential, which forces ϕ to the attractors at ± 1. Anisotropy is included in this equation by writing the interface mobility, τ, and width, W, as functions of the local normal vector, $\mathbf{n}$. Following Karma and Rappel,[5] we choose

$$W(\mathbf{n}) = W_0 a_s(\mathbf{n}); \quad \tau(\mathbf{n}) = \tau_0 a_s^2(\mathbf{n}) \qquad [11]$$

with the anisotropy function a, $(\mathbf{n})$ given now by

$$a_s(\mathbf{n}) = 1 - 3\epsilon_4 + 4\epsilon_4 \left[\frac{(\partial_x\phi)^4 + (\partial_y\phi)^4 + (\partial_z\phi)^4}{|\nabla\phi|^4} \right] \qquad [12]$$

As mentioned earlier, the constant parameter ϵ_4 fixes the strength of the anisotropy in the interface energy.

The important physical parameters in the simulations are the thermal diffusivity, α, capillary length, d_0, and surface tension anisotropy, ϵ_4. The phase-field model introduces the additional nonphysical parameters λ, W_0 and τ_0. Karma and Rappel[5] presented an asymptotic analysis to show the relations between the parameters such that the phase-field model converges to the sharp-interface model. In particular, for zero-interface kinetics, we have

$$\lambda = 1.5957 \frac{D\tau_0}{W_0^2}; \quad d_0 = 0.8839 \frac{W_0}{\lambda} \qquad [13]$$

where the numerical constants come from the asymptotic analysis. Simulations carried out over a wide range of values for D and d_0 produce similar results, when appropriately scaled, i.e., lengths are scaled on d_0, time is scaled on d_0^2/D, and velocities are scaled on D/d_0. This allows us to use computationally convenient values for D and d_0, while being able to compare our results with experimental observations by rescaling the results using the physical values of these parameters. We distinguish the physical values of D and d_0 from the corresponding computational ones by designating the latter as $\tilde{D}$ and $\tilde{d}_0$. In particular, it is advantageous to use relatively large values for $\tilde{D}$ because the dendrite evolves more quickly in that case.

We solve the 3-D flow equations using the semi-implicit approximate projection method,[23] a predictor-corrector method that can solve Eqs. [7] and [8] effectively, especially for large 3-D problems, using relatively small amounts of memory. For a detailed discussion of the algorithm, the reader is referred to the original article,[23] and for a detailed description of the parallel, adaptive finite-element implementation, see Jeong et al.[19]

The equations are solved in a segregated fashion, using an implicit time-stepping scheme, except for the phase-field equation, which we solve explicitly. The grid is adapted so that it is finest in the vicinity of the interface, where the grid spacing, Δx, must resolve the interface width, W_0, to a much coarser mesh far away, where all of the primitive fields vary slowly. The typical ratio of largest to smallest element size in our calculations is 512, but there is no inherent limit. Element refinement and fusion is done based on the value of an error estimator, computed from the solution within each element. The details of the procedure are given in Jeong et al.[19] and are not repeated here. The grid was adapted whenever the dendrite tip moved a predetermined distance, typically 0.4 W_0.

The basic problem that we solve places a small spherical seed at the centroid of a cube, with the axes of crystalline symmetry aligned with the cube edges. Earlier work has demonstrated that when the grid spacings are chosen as described earlier, grid anisotropy is minimal, and the seed orientation is merely a matter of convenience. Flow is introduced on the front face of the cube as a uniform velocity. The lateral faces are all assumed to be planes of symmetry, and the exit face has zero shear stress. The temperature on all faces of the computational domain is set to $-\Delta$, and we always use a domain of edge length, L_B, sufficiently large
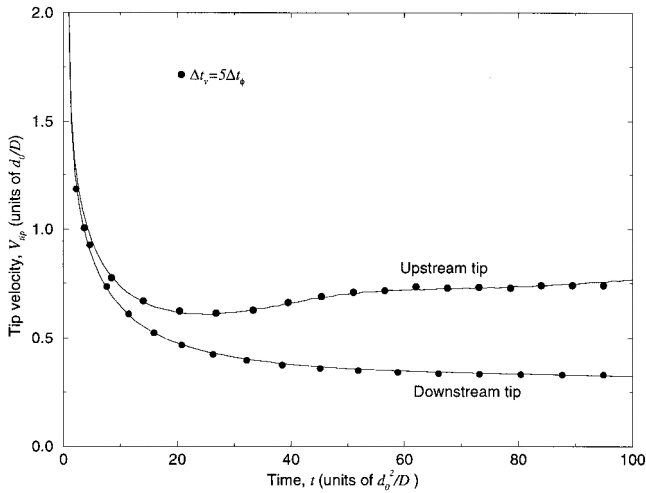
Fig. 1—Evolution of the dendrite-tip velocity for $r = 1$ (solid curves) and $r = 5$ (dashed curves with symbols), showing that the results are indistinguishable for the two cases. For this simulation, $\Delta = 0.55$, $\epsilon_4 = 0.05$, $\Delta t_{\theta\phi} = 0.016$, and $\Delta x_{min} = 0.8$.
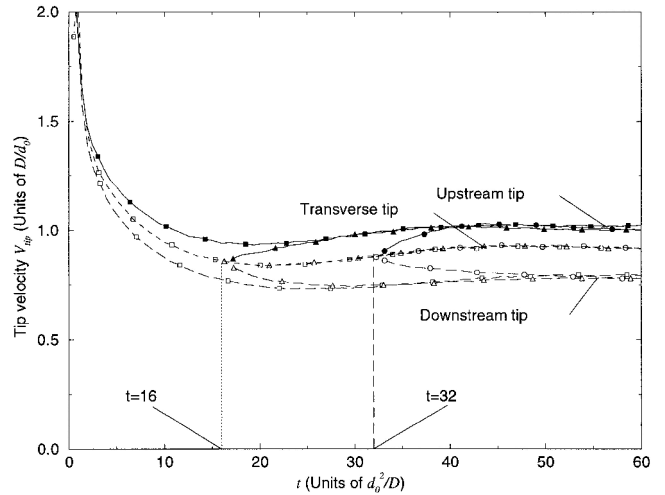

Fig. 2—Evolution of the dendrite-tip velocity for simulations started with flow, compared to simulations with fluid flow applied to a precursor seed grown without fluid flow up to two different times, $t = 16$ and $t = 32$. The other simulation parameters are the same as those given in Fig. 1.

that the thermal and velocity boundary conditions do not affect the result.

A convenient measure of the results is to track the evolution of the tip velocity and tip radius in the various directions. Simulations in two-dimensions[11] and three dimensions[19] showed that the tip velocity is increased on the leading arm, decreased on the trailing arm, and essentially unchanged on the transverse arms. We introduced a few "tricks" to speed up the calculations, and these are described now, using the leading and trailing tip velocities as indicators of the validity of these techniques.

We use a different time-step size to solve the various equations. The phase-field and temperature equations are solved using the minimum time-step, $\Delta t_{\theta\phi}$, and the fluid-flow equations are solved using a larger time-step, Δt_v. The physical basis for this choice is that the interface moves very slowly relative to the fluid, and thus, the motion of the interface does not strongly affect the flow field. Figure 1 shows an example of the evolution of the tip velocity using different time-step ratios, $r = \Delta t_v / \Delta t_{\theta\phi}$. The results were indistinguishable for values of r up to about 10 for relatively high speed growth and up to a ratio of 25 for very low speed growth, such as in SCN at low Δ. This provides a substantial computational savings compared to using a single time-step for all of the fields.

To further reduce computation time, we also use a technique where we start the computations with flow using a seed that had been grown to a small, but finite size without flow. Figure 2 shows the evolution of the dendrite-tip velocity for a dendrite simulated in this way, compared to the case where the flow was imposed at the beginning of the simulation. It can be seen that the tip velocity for a dendrite started from the precursor seed quickly recovers to the solution where flow was present from the beginning, and the results are indistinguishable. The dendrite-tip radius shows the same trend.

III. RESULTS

The simulations we report in this section were run to examine the role of fluid flow on dendrite growth at low Δ,

Table I. Parameters for Simulations Reported in This Section

Case	ϵ_4	Δ	U_∞ (cm/s)
1a	0.0055	0.04	0
b			0.5
c			1.0
2a	0.025	0.05	0
b			0.12
c			0.24
d			0.60

for comparison with experiments. We present results for the cases shown in Table I. The value of $\epsilon_4 = 0.0055$ corresponds to SCN, while $\epsilon_4 = 0.025$ corresponds to PVA. We note that these values have not been corrected for grid anisotropy. Karma and Rappel[5] give a correction for grid anisotropy where $\epsilon_{eff} = \epsilon_4 - (\Delta x_{min}^2/240)$. The grid-anisotropy correction for the finite-element form seems to be somewhat smaller,[6] but the results presented subsequently should nevertheless be viewed as approximate in this sense.

The simulations were run on a variety of machines: Sun (Mountain View, CA) Ultra-2/200 MHz, IBM (Armonk, NY) RS/6000 7043 Model 260, and SGI (Mountain View, CA) Origin 2000 multiprocessor machines. Comparisons of central processing unit (CPU) time for the various cases are, therefore, not meaningful. The parallel runs on the SGI Origin 2000 were usually made as a series of restart/batch jobs to optimize throughput in the queuing system. Statistics for one run (Case 1c), which should be considered representative, are that the run took 2496 CPU hours on 32 processors, 101 clock hours (average parallel efficiency of 77 pct), and used about 2 Gb of memory distributed over the 32 processors.

A. *Succinonitrile*

The evolution of ρ_{tip}, V_{tip}, and σ^* for the upstream arm for the SCN simulations are given in Figure 3. The computed
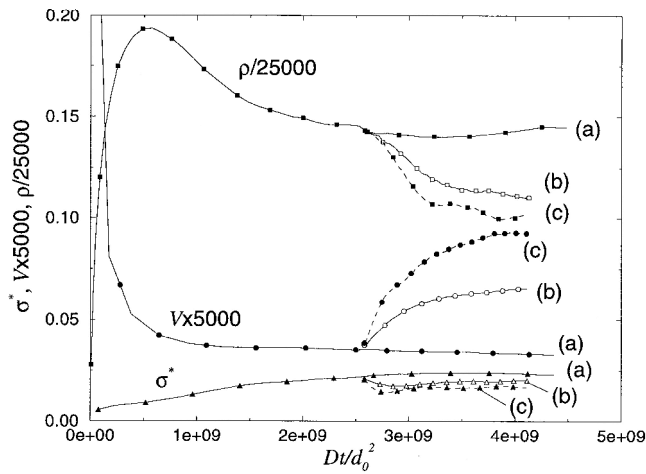
Fig. 3—Evolution of the tip radius (in units of d_0), tip velocity (in units of D/d_0), and selection constant σ^* for the upstream dendrite tip for three cases corresponding to succinonitrile solidification. The data have been multiplied by arbitrary constants for convenience of having them appear on one graph. The cases correspond to (a) no flow, (b) $U_\infty = 0.5$ cm/s, and (c) $U_\infty = 1$ cm/s.

Table II. Comparison of Computed and Experimental Tip Parameters for Succinonitrile

	U_∞ (cm/s)	V_{tip}/V_{tip}^0	ρ_{tip}/ρ_{tip}^0	σ^*/σ_0^*
Experimental	1.0	2.2	0.6	1.4
Calculated		2.6	0.72	0.8
Experimental	0.5	1.7	0.71	1.2
Calculated		2.1	0.71	0.95

values of ρ_{tip} and V_{tip} have been multiplied by arbitrary scales for the convenience of plotting them together on one graph. The seed was grown without flow up to $\tilde{D}t/\tilde{d}_0^2 = 2.5 \times 10^9$, and then the flow was started. For this simulation, we have $\tilde{d}_0 = 4.775 \times 10^{-3}$, $\tilde{D} = 116$, $W_0 = 1$, $\tau_0 = 1$, $\Delta x_{min} = 0.9$, $L_B = 29,491.2 \; (= 2^{15} \Delta x_{min})$, $\Delta t = 0.02$, and Pr = 23.1. The ratio $r = \Delta t_v/\Delta t_\phi$ was 25 in these simulations.

Figure 3 shows that V_{tip} increases dramatically, and ρ_{tip} decreases dramatically, immediately as the flow is started. The simulations do not appear to have reached a final steady state, but the temporal variation is small at the end of the simulations. (The simulations were terminated when the mesh size grew to about 450,000 nodes).

The selection constant, σ^* reaches its final value much more quickly than either V_{tip} or ρ_{tip}, which is also characteristic of calculations in the absence of flow. We find that σ^* decreases slightly with flow.

Table II compares the computed values of ρ_{tip}, V_{tip}, and σ^* with those obtained experimentally by Lee et al.[13] The results are presented as ratios of the final value in the simulations to the corresponding value without flow. Note that our simulations are not fully converged, so the values of V_{tip}^0 and ρ_{tip}^0 are different in the simulations than in experiments, although σ_0^* is the same for both. Whereas the ratios of tip velocities and tip radii are quite similar in the simulations and the experiments, the trends in σ^* are opposite, i.e., we find σ^* to be a weakly decreasing function of the far-field velocity, while Lee et al. found σ^* to be an increasing function of U_∞.

(a) $U_\infty = 0$ (b) $U_\infty = 0.5$ cm/s
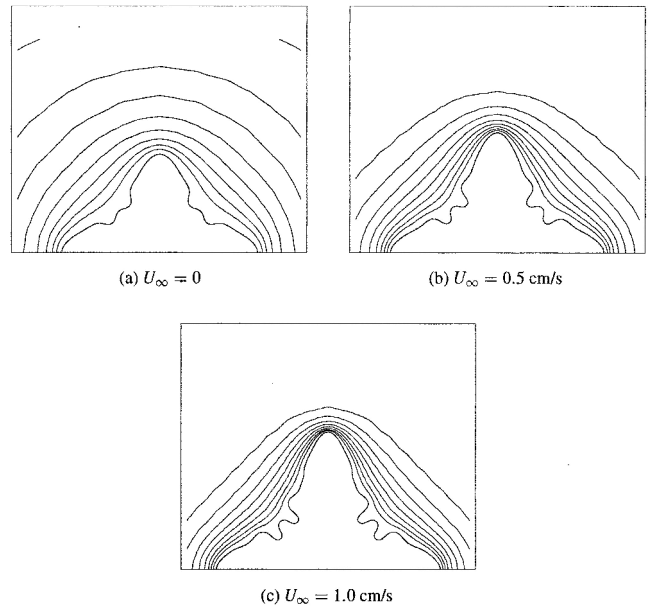
(c) $U_\infty = 1.0$ cm/s

Fig. 4—(a) through (c) Interface position and isotherms around the growing dendrite tip for SCN at $dt/d_0^2 = 4.1 \times 10^9$. Isotherms range from -0.036 to -0.008 in increments of 0.004. The flow from infinity originates from the top of the figure.
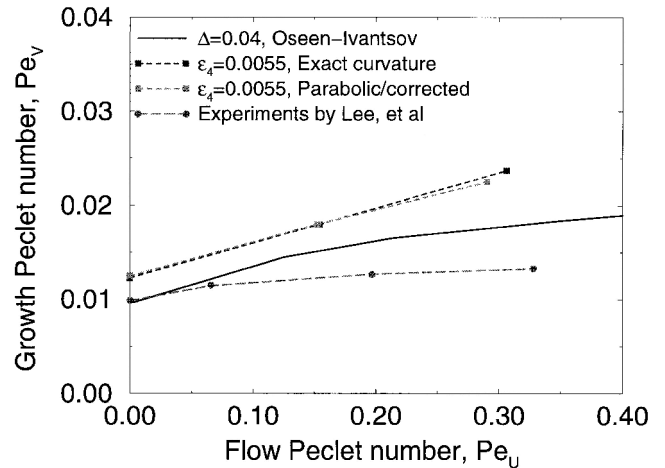

Fig. 5—Experimental and computational results for SCN, compared to the Oseen–Ivantsov transport solution.

The computed temperature field around the upstream tip is shown in Figure 4. The nascent sidebranch in Case 1c begins to appear at about $\tilde{D}t/\tilde{d}_0^2 = 3.5 \times 10^9$, and there is a corresponding perturbation in the tip velocity and tip radius (Figure 3.)

Note that σ^* remains relatively constant. The isotherms are advected by the flow, effectively increasing the temperature gradient ahead of the dendrite, and this leads to the increase in velocity of the dendrite tip.

Finally, it is in instructive to compare the results of the calculations with the solution of Beaghton and Saville. Although there is no unique state determined by their theory, the computed solution might be expected to follow their transport solution. Figure 5 shows plots of the growth Péclet number, $Pe_v = \rho_{tip} V_{tip}/\alpha$, vs the flow Péclet number, $Pe_u = \rho_{tip} U_\infty/\alpha$, for the experiments of Lee et al., our calculations,
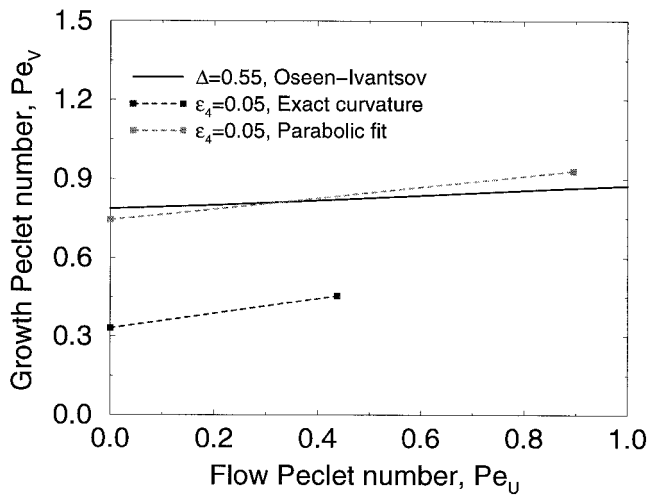
Fig. 6—Computational results for PVA at $\Delta = 0.55$, compared to the Oseen–Ivantsov transport solution.

Fig. 7—Evolution of the tip radius (in units of d_0), tip velocity (in units of D/d_0), and selection constant σ^* for the upstream dendrite tip for three cases corresponding to pivalic acid solidification. The data have been multiplied by arbitrary constants for the convenience of having them appear on one graph. The cases correspond to (a) no flow, (b) $U_\infty = 0.12$ cm/s, (c) $U_\infty = 0.24$ cm/s, and (d) $U_\infty = 0.60$ cm/s.

and the Oseen–Ivantsov solution. When the tip radius is computed using the exact computed shape of the dendrite, the results are quite far from the Oseen–Ivantsov solution. Beckermann et al.[11] showed that the tip radii should be corrected to compute a smooth paraboloidal shape near the tip for comparison to the transport solution. For this case, however, because the tip is so broad, the shape correction has almost no effect.

While the trends are similar, none of the curves match very well. This is important because it shows that neither the experiments nor the calculations match the transport solution for an isolated paraboloid of revolution. We believe that the explanation for this is that neither the computed nor experimental dendrites are well approximated as paraboloids (Figure 4), and therefore, the temperature field should not be expected to match the transport solution. It is also possible that the transverse arms affect the flow, an effect not accounted for at all in the Oseen–Ivantsov theory. We observed this phenomenon in diffusive growth at low Δ.[24]

B. Higher Anisotropy and PVA

At high anisotropy ($\epsilon_4 = 0.05$) and high undercooling ($\Delta = 0.55$), our results are similar to those reported by Beckermann et al., whose simulations were done in two-dimensions, but were otherwise similar to our 3-D analyses. The results are compared to the Oseen–Ivantsov solution in Figure 6, where reasonable agreement is found. Notice that in this case, where the dendrite tip is much sharper than it was for SCN, the parabolic-tip curvature correction brings the results into agreement with the Oseen–Ivantsov transport solution. This occurs because at high values of ϵ_4 and Δ the computed shape tends to look much more like the isolated paraboloid in the analytical solution than it does for smaller values of the parameters.

We also considered several cases with anisotropy $\epsilon_4 = 0.025$, corresponding to PVA. We note that we cannot compare these calculations directly with the experiments of Bouissou et al. for several reasons. Their experiments were performed in an alloy system, and at present, we compute only for pure materials. Further, their experiments were performed by growing dendrites in a narrow gap, much thinner than the boundary layers in that direction for a freely growing dendrite. We will examine this case in a later article.
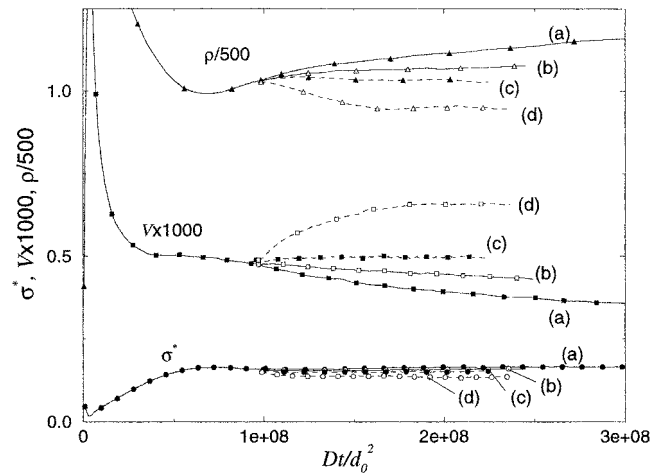

(a) $U_\infty = 0$

(b) $U_\infty = 0.12$ cm/s

(c) $U_\infty = 0.24$ cm/s
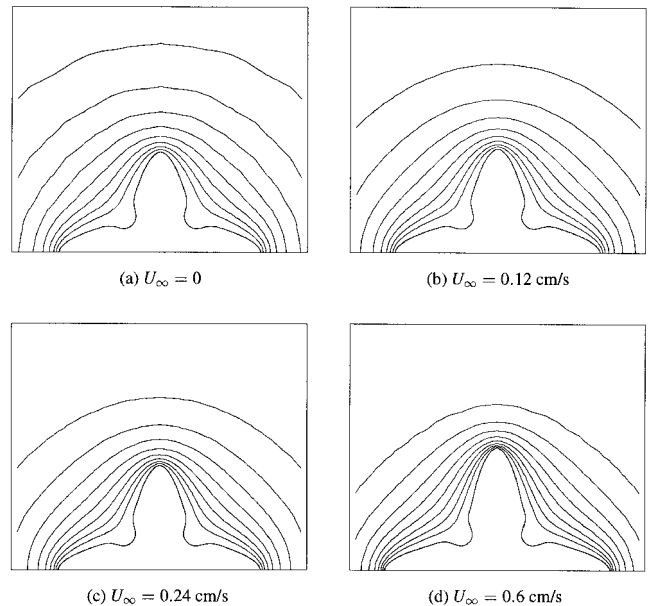
(d) $U_\infty = 0.6$ cm/s

Fig. 8—(a) through (d) Interface position and isotherms around the growing dendrite tip for PVA at $dt/d_0^2 = 2.3 \times 10^8$. Isotherms range from -0.045 to -0.01 in increments of 0.005. The flow from infinity originates from the top of the figure.

For this simulation, we have $\tilde{d}_0 = 1.385 \times 10^{-2}, \tilde{D} = 40$, $W_0 = 1$, $\tau_0 = 1$, $\Delta x_{\min} = 0.9$, $L_B = 14745.6 \, (= 2^{14} \Delta x_{\min})$, $\Delta t = 0.15$, and Pr $= 134.92$. The ratio $r = \Delta t_\nu/\Delta t_\phi$ was 5 for the PVA simulations.

The results of the calculations for PVA at low Δ are illustrated in Figures 7 through 9. Similar trends are observed for PVA as in SCN, i.e., the dendrite-tip velocity increases and tip radius decreases as U_∞ increases. Once again, σ^* is a weakly decreasing function of U_∞, which reaches a steady value much sooner than either ρ_{tip} or V_{tip}. The isotherms, illustrated in Figure 8, are once again advected by the flow, but the tip shape is much smoother for PVA than for SCN;
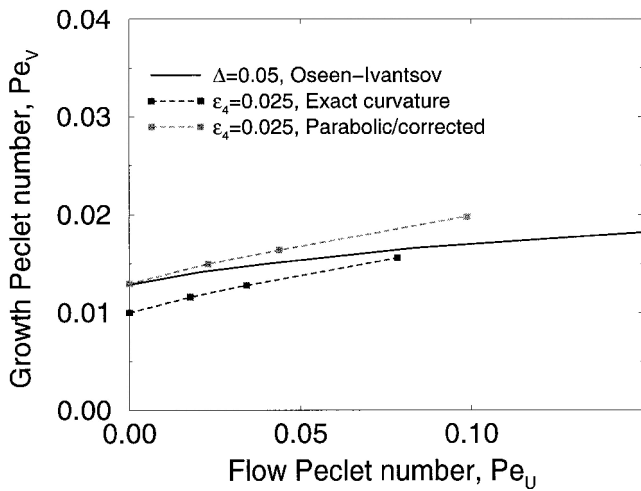
Fig. 9—Computational results for PVA, compared to the Oseen–Ivantsov transport solution.
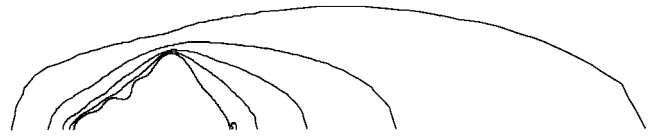

Fig. 10—Contours of flow speed around a solidifying SCN dendrite. The contours represent 0, 0.2, 0.4, 0.6, and 0.8 times U_∞. The flow clearly "sees" the entire dendrite, rather than just the tip. Note that in this figure, the flow from infinity originates from the left, rather than from the top, as in Figs. 4 and 8.

however, Figure 9 still shows systematic deviations from the Oseen–Ivanstov solution.

IV. DISCUSSION

The most important observation from our computations is that significant discrepancies exist between the analytical theory of Saville and Beaghton for an isolated branchless dendrite, our calculations, *and* the available experimental results. We believe that the source of these differences lies in the difference between the real shape of a growing dendrite, and the assumed branchless, isolated paraboloid.

Much has been made about the trend in the selection constant σ^* with increasing imposed flow. We find a very weak negative dependence of σ^* on U_∞, *i.e.*, σ^* decreases slightly as U_∞ increases. We note that even though σ^* is nearly constant, the tip velocity increases substantially, and the tip radius decreases significantly. Within the precision of our calculations, σ^* is essentially constant.

This result is consistent with the theory of Bouissou and Pelcé. Consider our Case 1c: SCN growing with $\Delta = 0.04$ and $U_\infty = 1$ cm/s. Using the computed value for the tip radius for this case, $\rho_{tip} = 7.1$ μm, and other properties for SCN, the Reynolds number is computed to be Re = 0.03, from which we may determine $a(\text{Re})$ from Eq. [1] to be 0.16. We may read the values for Pe_v and Pe_u from the graph in Figure 5 to be 0.015 and 0.05, respectively. Thus, we have

$$a(\text{Re}) \frac{\text{Pe}_u}{\text{Pe}_v} = 0.05 \ll 1 \qquad [14]$$

and the theory predicts that σ^* is independent of U_∞.

Figure 5 showed significant deviations between the theory of Saville and Beaghton and *both* our calculations and the experiments of Lee *et al.*[13] We believe that the difference arises from the idealization of the dendrite as an isolated paraboloidal shape. For low Reynolds numbers, we expect to find a viscous boundary layer of thickness approximately

$$\delta_v \sim \frac{\nu}{U_\infty} = \frac{\rho_{tip}}{\text{Re}} \qquad [15]$$

ahead of any obstacle, including sidebranches and transverse

arms. For the example cited in the preceding paragraph, $\delta_v \sim 235$ μm. This is clearly larger than the distance to the transverse arms in our computations and probably also in the experiments. Thus, if the flow field is significantly different from the Oseen–Ivantsov solution, one cannot expect the results to match the theory. Figure 10 shows contours of constant speed for the case of SCN solidification, where one can clearly see that the flow reacts to the entire body of the dendrite, not just the tip. We note that this effect would be even more pronounced in two dimensions, where flow around the dendrite tip cannot occur.

Our conclusion from this is that both the experiments and the calculations are very difficult to perform in such a way as to satisfy the idealized conditions assumed in the theory, and this clouds our ability to make precise statements about the theory of tip selection under conditions of forced flow.

V. CONCLUSIONS

We have developed a 3-D, adaptive, parallel finite-element code to examine solidification of pure materials under conditions of forced flow. We have examined the effect of undercooling, surface-tension anisotropy, and imposed flow velocity on the growth. The flow significantly alters the growth process, producing dendrites that grow faster, and with greater tip curvature, into the flow. The selection constant σ^* decreases slightly with flow velocity in our calculations.

The results of the calculations agree well with the transport solution of Saville and Beaghton[9] at high undercooling and high anisotropy. At low undercooling, significant deviations are found. We attribute this difference to the influence of other parts of the dendrite removed from the tip on the flow field.

REFERENCES

1. G.P. Ivantsov: *Dokl. Akad. Nauk USSR*, 1947, vol. 58, pp. 1113.
2. E. Ben-Jacob, N. Goldenfeld, B.G. Kotliar, and J.S. Langer: *Phys. Rev. Lett.*, 1984, vol. 53, p. 2110.
3. D. Kessler, J. Koplik, and H. Levine: *Phys. Rev. A*, 1984, vol. 30, p. 3161.
4. E. Brener: *Phys. Rev. Lett.*, 1993, vol. 71 (22), pp. 3653-56.
5. A. Karma and W.-J. Rappel: *Phys. Rev. E.*, 1995, vol. 53, p. 3017.
6. N. Provatas, N. Goldenfeld, and J. Dantzig: *Phys. Rev. Lett.*, 1998, vol. 80, p. 3308.

7. S.H. Davis: *Theory of Solidification*, Cambridge University Press, Cambridge, United Kingdom, 2001.
8. S.-C. Huang and M.E. Glicksman: *Acta Metall.*, 1981, vol. 29, p. 1697.
9. D.A. Saville and P.J. Beaghton: *Phys. Rev. A*, 1988, vol. 37 (9), pp. 3423-30.
10. P. Bouissou and P. Pelcé: *Phys. Rev. A*, 1989, vol. 40, pp. 6673-80.
11. C. Beckermann, H.-J. Diepers, I. Steinbach, A. Karma, and X. Tong: *J. Comp. Phys.*, 1999, vol. 154, p. 468.
12. P. Bouissou, B. Perrin, and P. Tabeling: *Phys. Rev. A*, 1989, vol. 40 (1), pp. 509-12.
13. Y.-W. Lee, R. Ananth, and W.N. Gill: *J. Cryst. Growth*, 1993, vol. 132, p. 226.
14. R. Kobayashi: *Physica D*, 1993, vol. 63, p. 410.
15. A.A. Wheeler, W.J. Boettinger, and G.B. McFadden: *Phys. Rev. A*, 1992, vol. 45, p. 7424.
16. J.A. Warren and W.J. Boettinger: *Acta Metall. Mater. A*, 1995, vol. 43, p. 689.
17. A. Karma and W.-J. Rappel: *Phys. Rev. E*, 1995, vol. 53, p. 3017.
18. N. Provatas, N. Goldenfeld, and J. Dantzig: *J. Comp. Phys*, 1999, vol. 148, p. 265.
19. J.-H. Jeong, N. Goldenfeld, and J.A. Dantzig: *Phys. Rev. E*, 2001, vol. 64, pp. 041602-14, 2001.
20. M. Plapp and A. Karma: *J. Comp. Phys.*, 2000, vol. 165 (2), pp. 592-619.
21. R. Tönhardt and G. Amberg: *J. Cryst. Growth*, 1998, vol. 194, p. 406.
22. D. Juric: in *Modeling of Casting, Welding and Advanced Solidification Processes*, B.G. Thomas and C. Beckermann, eds., TMS-AIME, Warrendale, PA, 1998, pp. 605-12.
23. P.M. Gresho, S.T. Chan, M.A. Christon, and A.C. Hindmarsh: *Int. J. Num. Methods Fluids*, 1995, vol. 21, p. 837.
24. N. Provatas, J. Dantzig, and N. Goldenfeld: *Phys. Rev. Lett.*, 1998, vol. 80, p. 3308.